

Olfactory bulb coding of odors, mixtures and sniffs is a linear sum of odor time profiles

Priyanka Gupta^{1,2}, Dinu F Albeanu^{2,3} & Upinder S Bhalla¹

The olfactory system receives intermittent and fluctuating inputs arising from dispersion of odor plumes and active sampling by the animal. Previous work has suggested that the olfactory transduction machinery and excitatory-inhibitory olfactory bulb circuitry generate nonlinear population trajectories of neuronal activity that differ across odorants. Here we show that individual mitral/tufted (M/T) cells sum inputs linearly across odors and time. By decoupling odor sampling from respiration in anesthetized rats, we show that M/T cell responses to arbitrary odor waveforms and mixtures are well described by odor-specific impulse responses convolved with the odorant's temporal profile. The same impulse responses convolved with the respiratory airflow predict the classical respiration-locked firing of olfactory bulb neurons and several other reported response properties of M/T cells. These results show that the olfactory bulb linearly processes fluctuating odor inputs, thereby simplifying downstream decoding of stimulus identity and temporal dynamics.

Odors are carried through turbulent media (air or water), and the signals arriving at the olfactory sensors vary both in intensity and in duration¹. Active sampling behaviors, including sniffing, whisking and head movements, add further fluctuations to the signal^{2,3}. Animals routinely identify odors of interest (e.g., food or mates) and locate their source within a fluctuating, multi-odor background⁴⁻⁷. However, how the olfactory system integrates intermittent and multiplexed odor inputs to simultaneously extract identity and intensity of multiple odors, as well as the precise timing of their arrival, remains unknown.

Representation of odor identity is well characterized in the input layer (glomeruli) of the olfactory bulb (OB). Selectivity of individual olfactory receptor neurons (ORNs) for subsets of odors and conserved projections of ORNs to glomeruli give rise to distinct, odor-specific spatiotemporal activity patterns on the OB surface⁸⁻¹². Local microcircuits allow integration of inputs from multiple glomeruli, transforming the spatially distributed glomerular patterns into temporal codes at the level of individual M/T cells¹³. Phasic tuning of M/T cell responses to the respiratory cycle (respiration tuning)^{14,15} further increases the temporal diversity of odor responses¹⁶⁻¹⁸. The diverse, odor-specific latencies of M/T cell responses during respiration have been proposed as a substrate for coding odor identity (latency coding)¹⁹⁻²¹.

Odor stimuli themselves vary in time. This challenges a temporal framework for coding odor identity: how do M/T cells encode fluctuations within the stimulus, over and above the temporal shifts in their responses that encode odor identity? This is further complicated by other features of odor stimuli (e.g., variations in concentration or in composition of odor mixtures) that also temporally modulate M/T cell responses. For instance, increasing odor concentration recruits additional glomeruli^{8-10,12} and alters M/T cell firing patterns. At higher concentrations, M/T cells tend to not only fire earlier in the

respiratory cycle but also exhibit extended inhibitory responses^{16,22}. Similarly, temporal shifts in M/T cell firing with respect to the respiratory cycle have been shown to be characteristic of mixture responses^{16,23}. Although glomerular activity patterns in response to odor mixtures generally overlap with the respective individual odor activation maps in the glomeruli^{12,24}, neither the behavioral percepts^{25,26} nor the individual M/T cell firing patterns²³ are simple sums of the individual odor contributions.

An effective M/T cell encoding scheme is therefore highly constrained. It must retain simultaneous information about odor identity, intensity and timing, despite multiple observations of apparent spillover of identity, intensity and mixture information into the time domain.

Technical limitations²⁷ in controlling spatiotemporal dynamics of odor stimuli have posed constraints in the investigation of coding mechanisms for temporally patterned olfactory stimuli. Additional complexities induced by the periodic nature of respiration-driven odor sampling have restricted such *in vivo* studies mostly to insect systems.

Recent work has shown linear, temporal integration of inputs of individual odors in *Drosophila* ORNs^{28,29}. A few groups have explored summation properties of projection neurons (PNs, M/T cell analogs) in locust and fish olfactory systems, comparing responses of simultaneous and sequential presentation of two odors³⁰⁻³². These studies report nonlinear encoding at the levels of both individual and large numbers of PNs, proposing that odor identity is encoded in the time-trajectory of ensemble activity of PNs^{30,31,33}. Trajectories for binary mixtures are distinct from those of the components and depend nonlinearly on the sequence of odor presentation. In rodents, two studies examined M/T cells responses to static binary mixtures, reaching opposing conclusions about linearity of response summation^{16,23}. Summation of time-varying odor inputs has not been

¹National Centre for Biological Sciences, Bangalore, India. ²Cold Spring Harbor Laboratory, Cold Spring Harbor, New York, USA. ³Watson School of Biological Sciences, Cold Spring Harbor, New York, USA. Correspondence should be addressed to U.S.B. (bhalla@ncbs.res.in).

Received 6 October 2014; accepted 4 December 2014; published online 12 January 2015; doi:10.1038/nn.3913

explored, with the exception of one recent study in the locust olfactory system that also reported nonlinear summation of inputs within and across odors³⁴.

We used precisely controlled, arbitrary time-varying stimuli and respiration-decoupled odor sampling to investigate M/T cell responses to fluctuating inputs of individual odors and their binary mixtures, as well as across different concentrations of a given odor. In contrast to the results of previous studies, we have found that individual M/T cells respond to temporally interleaved inputs of individual odors and their mixtures in a surprisingly linear manner. This simple linear model accurately captures the odor-specific respiration tuning of M/T cells responses, a characteristic feature of respiring animals. Further, we show that latency coding of odor identity and temporal diversity of M/T cells across the respiration cycle are emergent properties of linear summation.

RESULTS

Precisely controlled time-varying odor stimuli

To characterize M/T cell responses to time-varying odor stimuli, we developed an odor delivery system capable of generating odor stimuli of arbitrary temporal structure at fast time scales (~20 Hz) (Fig. 1a,b). Serial air dilutions of saturated odor vapor and careful selection of carrier flow rates conferred linear control of output odor concentration, fast kinetics and high reproducibility across trials. Importantly, the system maintained stable flow rates during air-odor transitions so as to avoid mechanosensory ORN activation³⁵ (Fig. 1b, Supplementary Fig. 1 and Online Methods).

In mammals, odor sampling is coupled to inhalation, which itself results in temporal patterning of odor inputs. To maintain direct control on the stimulus amplitude and timing, we used double tracheotomy¹⁶ to decouple odor sampling from respiration in anesthetized rats (Fig. 1c and Online Methods).

We recorded M/T cell responses to time-varying stimuli using extracellular tetrodes (Fig. 1c,d). Stimulus patterns included individual pulses of variable duration (50–2,000 ms), paired pulses of varying interpulse intervals (50–1,000 ms) and pseudo-random fluctuating patterns³⁴ (Online Methods). M/T cells showed odor-specific excitatory and/or inhibitory responses for each stimulus pattern (Fig. 1d). Consistent with previous studies, we did not observe respiratory modulation of responses in the tracheotomized animals^{16,36}.

M/T cells linearly sum odor inputs in time

For each odor-cell pair, we estimated an odor kernel that best described the response of the cell to a brief odor pulse (Fig. 2a,b). To this end, we used half of the stimulus-response pairs recorded for a given cell (training data set) and minimized the least-square error between the experimentally observed and predicted response for these select stimuli (Online Methods). We found that the response of the cell to other arbitrary time-varying patterns of the same odor (cross-validation data set) was reliably predicted by convolving the estimated odor kernel with the odor waveform, measured by a photoionization detector²⁷ (PID) (Fig. 2c).

The model reliably predicted both excitatory and inhibitory odor responses (Fig. 2c). Predicted inhibitory responses appeared as negative firing rates and overlapped with the experimentally observed periods of zero firing (Supplementary Fig. 2). Interestingly, the amplitude of inhibitory responses was unmasked during the overlap of the excitatory and inhibitory components of the response evoked by an odor when more than one pulse was delivered in close succession at different interpulse intervals (Supplementary Fig. 2). Consistent with this idea, we found that kernels could be estimated from the response to a single pseudo-randomly fluctuating pattern spanning a large range of interpulse intervals.

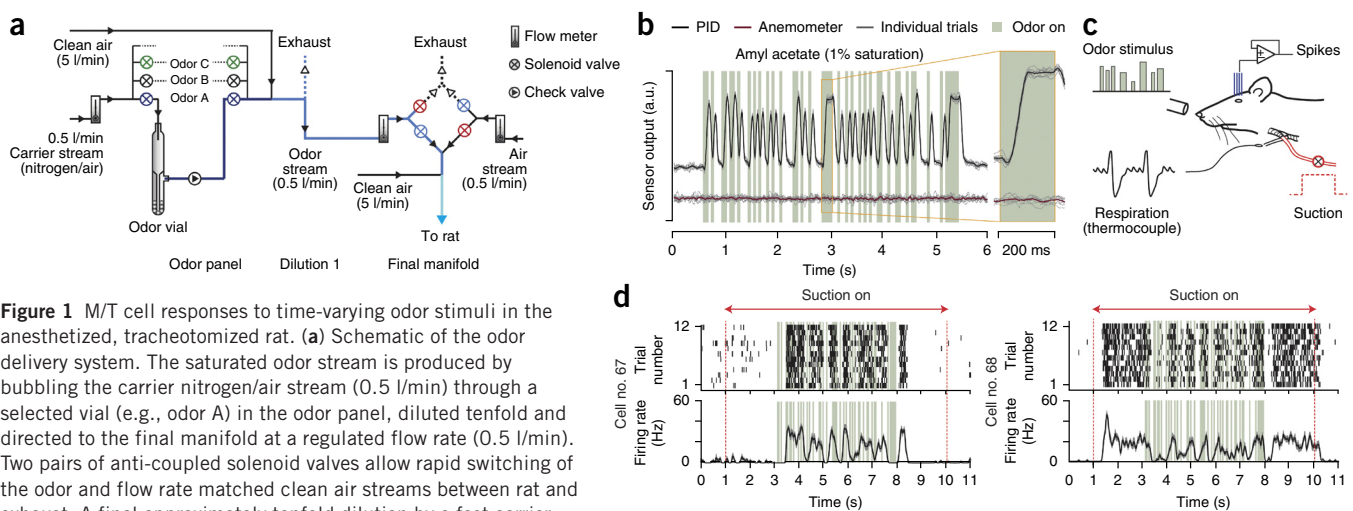
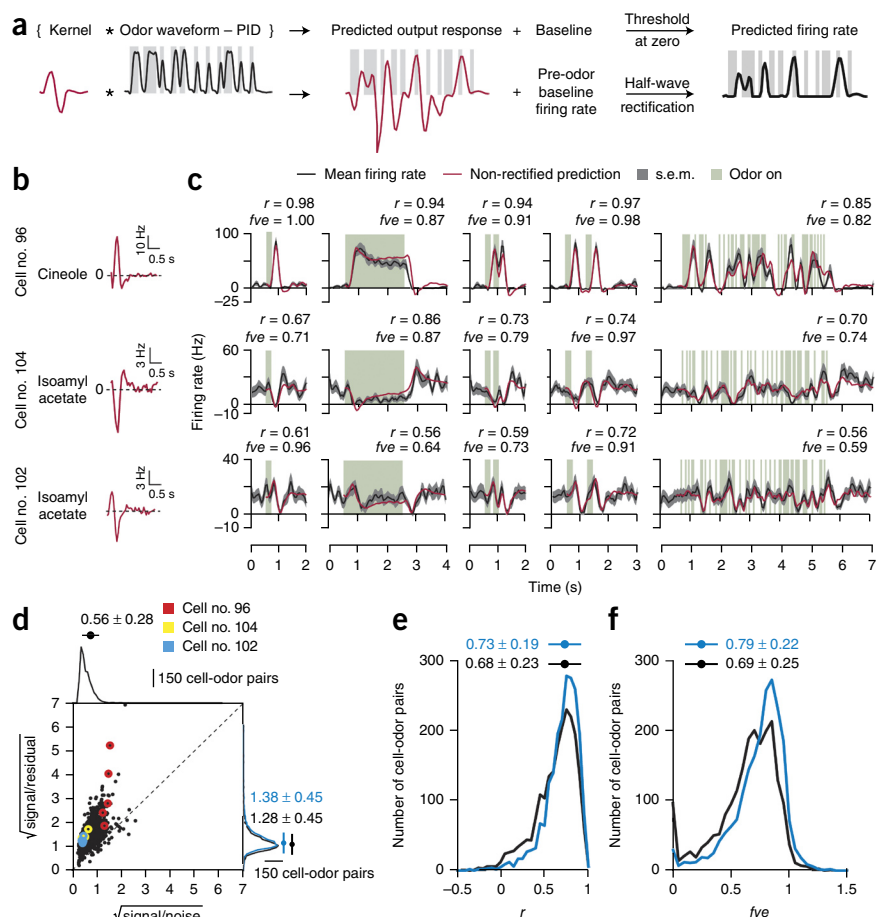


Figure 1 M/T cell responses to time-varying odor stimuli in the anesthetized, tracheotomized rat. **(a)** Schematic of the odor delivery system. The saturated odor stream is produced by bubbling the carrier nitrogen/air stream (0.5 l/min) through a selected vial (e.g., odor A) in the odor panel, diluted tenfold and directed to the final manifold at a regulated flow rate (0.5 l/min). Two pairs of anti-coupled solenoid valves allow rapid switching of the odor and flow rate matched clean air streams between rat and exhaust. A final approximately tenfold dilution by a fast carrier stream (5 l/min) ensures rapid kinetics and constant output flow. Pairs of valves simultaneously on (red) or off (blue) are indicated in the same color. **(b)** Observed output profile for amyl acetate (1% saturation) for a pseudo-random sequence of odor pulses. Vertical green bars mark odor valve on periods. Black and red lines show simultaneously measured, average read-outs of a PID (black) and anemometer (red) (sampling rate, 1 KHz). Sensor outputs were measured in volts and are plotted here in arbitrary units (a.u.). Gray lines show individual trials (10 trials). Inset shows enlarged view of a 200-ms-long pulse within the sequence. **(c)** Schematic of the experimental setup for extracellular single-unit recordings from M/T cells in anesthetized, tracheotomized rats. Tetrodes (blue) were inserted in the olfactory bulb to record M/T cell responses to time-varying odor stimuli delivered at the snout via the odor delivery system shown in **a**. Nasal airflow through the upper trachea was controlled via active suction and gated by a digitally controlled solenoid valve (red). Dotted line represents ON-OFF state of suction valve. Respiration was monitored by a thermocouple. **(d)** Firing rate response of two simultaneously recorded M/T cells to the fluctuating stimulus pattern of amyl acetate shown in **c**. Raster plots show spiking output (12 trials). Black bands represent individual spikes, plotted at 1-ms resolution. Peristimulus time histograms (PSTHs) show the corresponding average firing rate (black). Gray bands in the PSTH indicate one s.e.m. Dashed red lines mark period with suction on. Green bars mark odor ON periods. For **c,d**: M/T cells, $n = 130$; rats, $n = 34$; odors, $n = 9$.

Figure 2 Linear summation of inputs predicts M/T cell responses to time-varying odor patterns. **(a)** Schematic of the linear model. The M/T cell response is calculated by convolving the odor kernel with the odor waveform (measured via PID). Negative firing rates are rectified after addition of the pre-odor baseline. Vertical bars mark odor ON periods. **(b)** Estimated odor kernels of three example M/T cells. Odors used are indicated on the left of each kernel. Odors were delivered at 1% saturation. **(c)** Comparison of model predictions and observed responses of the M/T cells in **b** to various time-varying odor stimuli. Vertical green bars mark odor on periods. Black lines show the observed mean firing rate across 12 trials. Gray bands indicate s.e.m. Red lines shows the non-rectified prediction from the model using the estimated kernels shown in **b**. M/T cells, $n = 76$; odors, $n = 8$; stimulus patterns, $n = 1,114$.

(d) Summary plot showing comparison of the residual error between predicted and observed firing rates with the trial-to-trial variation (noise) in the observed response. Each black dot represents one stimulus pattern in a scatter plot of $\sqrt{\text{signal/residual}}$ against $\sqrt{\text{signal/noise}}$. Points lying above the slope of unity (dashed black line) indicate that deviation of the fit from the mean is less than the trial-to-trial variability in the response. M/T cells, $n = 130$; odors, $n = 9$; stimulus patterns, $n = 2,062$ stimulus patterns. Colored circles correspond to the responses of the three example M/T cells shown in **c** (red = cell no. 96, yellow = cell no. 104, blue = cell no. 102). Marginal histograms show distribution of $\sqrt{\text{signal/noise}}$ (top) and $\sqrt{\text{signal/residual}}$ (right) across all cell-stimulus pairs. Black histogram on right corresponds to residuals obtained when the responses were predicted by cross-validation. Blue histogram on right corresponds to residuals obtained when the predicted responses were part of the training data set. \pm indicate median and s.d. **(e)** Summary histogram of the correlation coefficient (r) between the predicted and observed mean firing rate response for all cell-stimulus pairs. Histograms correspond to the correlations obtained for cross-validated (black) and training data sets (blue). \pm indicate median and s.d. **(f)** Summary histogram of the fraction of variance explained (fve ; Online Methods) by the model across all cell-stimulus pairs. Histograms correspond to the correlations obtained for cross-validated (black) and training data sets (blue). \pm indicate median and s.d.



As a first test of the model's performance, we compared the prediction error (residual) to the intertrial variability (noise) in the observed response, using a published metric³⁴ (Online Methods). We calculated prediction error as the mean squared difference between the predicted and observed mean firing rate for a given stimulus pattern. 95% of our predictions had a residual error smaller than the intertrial noise (1,962 out of 2,062; left tail t -test, $P > 0.05$; **Supplementary Fig. 3a**), indicating that the predicted firing rate approximated the average firing rate response of the cell within one s.d. (**Fig. 2d**).

Given the low average signal-to-noise ratio in M/T cell odor responses (0.56 ± 0.28 , median \pm s.d., **Fig. 2d**), residuals smaller than the intertrial noise may not necessarily reflect a good estimation of the mean response profile. To obtain a more intuitive estimate of the model's performance, we calculated: (i) the correlation coefficient (r) between the predicted and observed response (Online Methods) and (ii) the fraction of stimulus-related variance in the observed mean response explained by the model (fraction of variance explained (fve); Online Methods). Model predictions showed high correlation with the observed response (0.68 ± 0.23 , median \pm s.d., **Fig. 2e**), explaining on average 70% of the response variance (0.69 ± 0.25 , median \pm s.d., **Fig. 2f**), even for M/T cell odor responses with low signal-to-noise ratio (**Supplementary Fig. 3b**). The correlation between the model predictions and observed mean firing rate response was consistently

higher than the pairwise correlation across individual trials (**Supplementary Fig. 3b**). Together, these metrics (**Fig. 2d–f**) indicate that a linear model is a better estimator of the mean response of the cell than individual trials.

Thus, linear summation of impulse response kernels accounts for the majority of the variance in observed M/T cell responses to fluctuating odor stimuli.

Most M/T cell odor kernels are concentration dependent

For a subset of cells ($n = 19$), we repeated the stimulus series at multiple concentrations to examine whether responses remained linear across a larger odor concentration range. For each odor-cell pair, we interleaved presentations of the same stimulus patterns at two (8 cell-odor pairs) or three (11 cell-odor pairs) different peak odor concentrations (ranging from 0.4% to 3.5% saturation) (**Supplementary Fig. 4**). We estimated kernels independently at each concentration using normalized stimulus (PID) waveforms (**Fig. 3a**). The PID waveform for a given concentration was normalized by the maximum PID signal observed across all stimulus patterns presented for that particular concentration. In this scenario, if M/T cell odor responses remained linear across concentrations, the kernels estimated at different concentrations would be identical in shape and differ in amplitude proportional to the relative stimulus strengths at the different

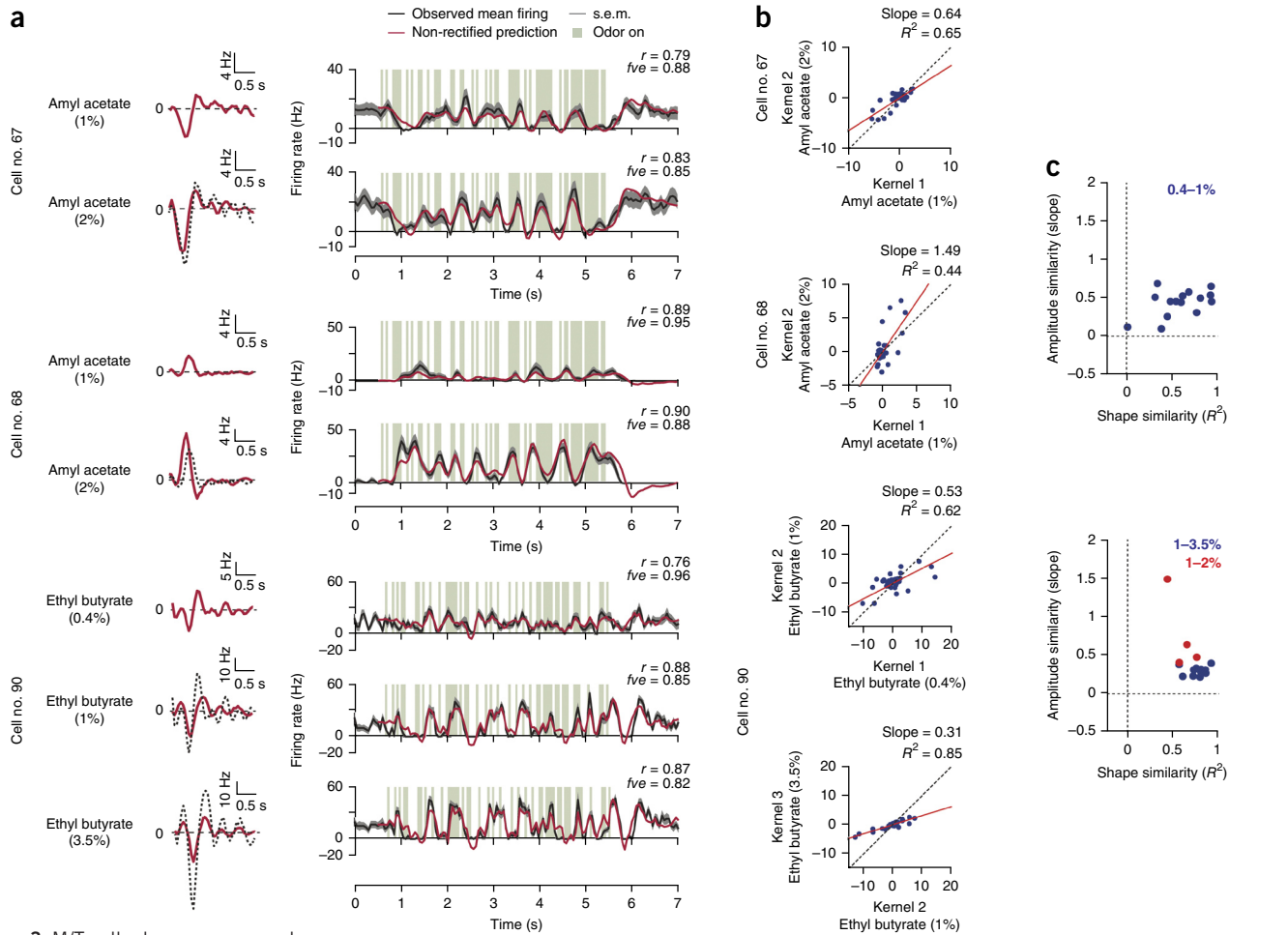


Figure 3 M/T cell odor responses scale nonlinearly with odor concentration while maintaining linearity across time.

(a) Estimated response kernels (left) and observed and predicted firing rate responses (right) of three M/T cells across different concentrations of the same stimulus pattern. Response kernels (red) estimated independently at each odor concentration (left). Dotted black lines show the expected kernel shape at the higher concentration by linear scaling of the kernel at the lower concentration. Odors and concentrations used are indicated along with each kernel. Observed and predicted responses of the M/T cells in pseudo-random odor pulse sequences delivered at different peak stimulus concentrations (right). Vertical green bars mark odor on periods. Black lines show the observed mean firing rate across 12 trials. Gray bands indicate s.e.m. Red lines show the non-rectified prediction from the model using the estimated kernels in **a**. (b) Point-by-point comparison of pairs of kernels estimated at two odor saturations. Panels correspond to kernel pairs shown in **a**. Red line shows the best-fit line from linear regression. The slope of the regression line indicates the concentration-dependent scaling of kernel amplitudes. Dashed black line indicates the slope of unity. Slopes of 1, <1 and >1 indicate linear, sublinear and supralinear scaling, respectively. Regression statistic (R^2) indicates degree of similarity in kernel shape, independent of scaling. R^2 of 1 indicates identical kernel shapes at the two concentrations. (c) Scatter plot of amplitude similarity (slope) and shape similarity (R^2) for all pairs of kernels estimated at two odor concentrations. Scatter along x axis represents differences in kernel shapes. Scatter along y axis represents concentration-dependent amplitude scaling. Left graph corresponds to kernel pairs at 0.4 versus 1% odor saturation (odor-cell pairs, $n = 15$). Right graph corresponds to kernel pairs at 1 versus 2% odor saturation (red dots; odor-cell pairs, $n = 4$) or 1 versus 3.5% odor saturation (blue dots; odor-cell pairs, $n = 11$). (d) Summary plot showing comparison of the residual error between predicted and observed firing rates with the trial-to-trial variation (noise) in the observed response at different odor saturations. Each dot represents one stimulus-concentration pair in a scatter plot of $\sqrt{\text{signal/residual}}$ against $\sqrt{\text{signal/noise}}$. Points lying above the slope of unity (dashed black line) indicate that deviation of the fit from the mean is less than the trial-to-trial variability in the response. Stimuli, $n = 320$; concentration pairs, $n = 30$; M/T cells, $n = 19$. Marginal histograms show distribution of $\sqrt{\text{signal/residual}}$ (top) and $\sqrt{\text{signal/noise}}$ (right) across all cell-stimulus pairs at different odor saturations. \pm indicate median and s.d. (e) Summary histogram of r between the predicted and observed mean firing rate response for all cell-stimulus pairs at different odor saturations. (f) Summary histogram of fve by the model across all cell-stimulus pairs at different odor saturations. For **d–f**, red = 0.4% saturation; blue = 1–2% saturation; purple = 3.5% saturation. \pm indicate median and s.d., and n.s. indicates no significant pairwise difference. Two-sided Wilcoxon rank sum test, $P > 0.05$.

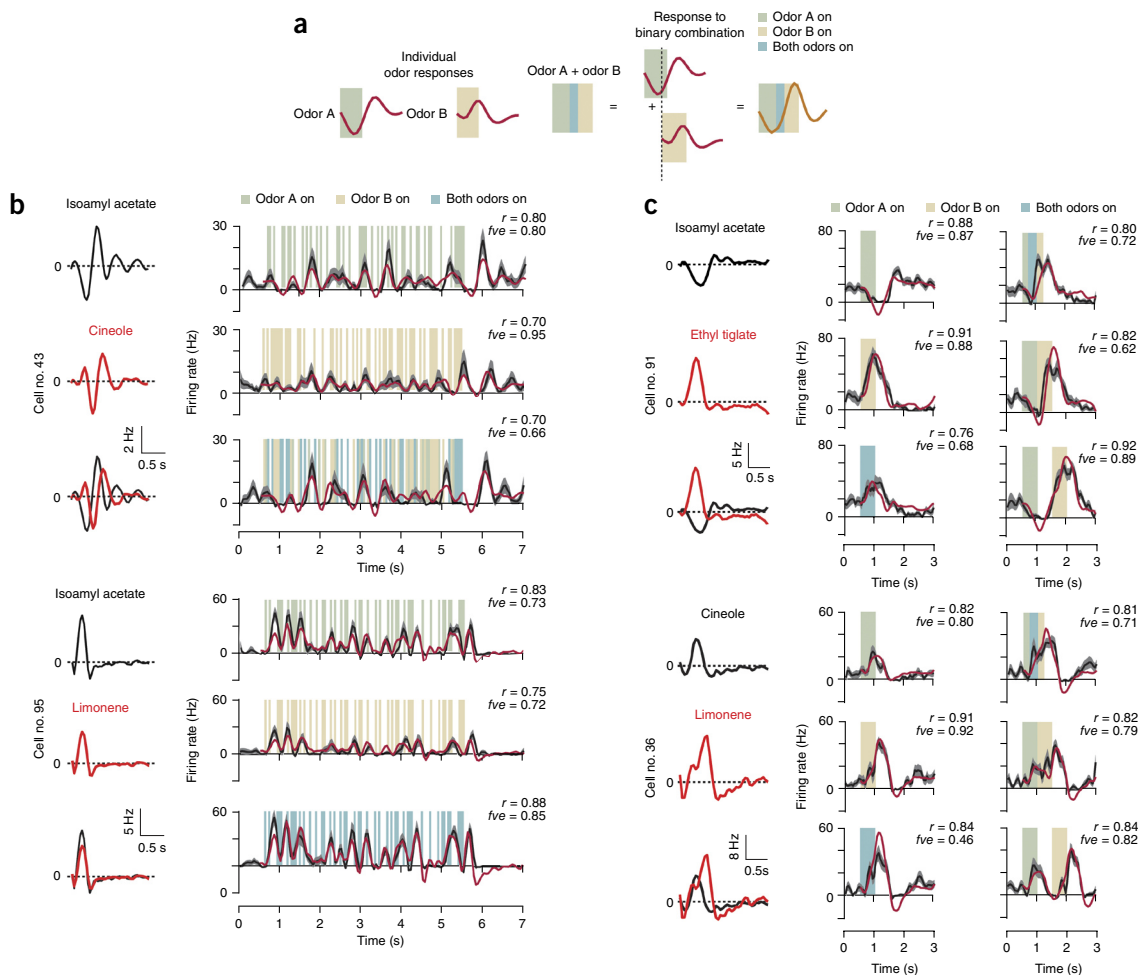
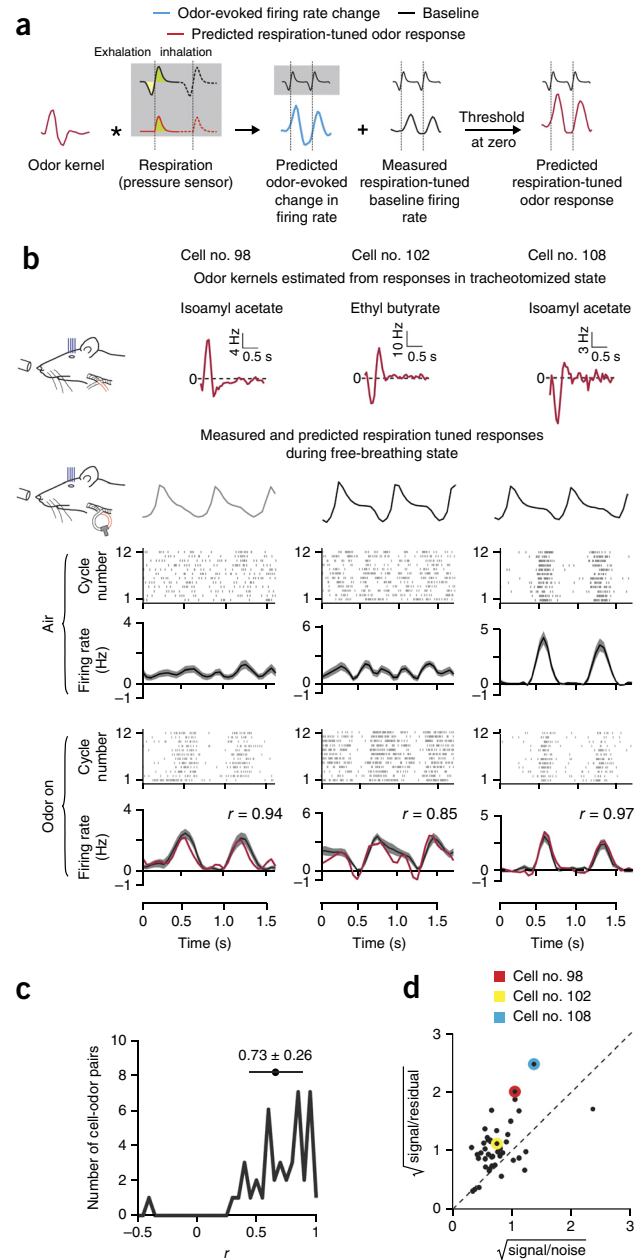


Figure 4 M/T cell response to binary odor mixtures is a sum of responses to the components. **(a)** Schematic of the summation model for binary odor stimuli. M/T cell response to binary combinations of odor A and B was calculated as a sum of predicted responses to each odor stimulus presented individually. **(b)** Estimated odor kernels (left) and observed and predicted firing rate responses (right) of two M/T cells to pseudo-random fluctuating patterns of two odors presented individually as well as simultaneously in the form of fluctuating binary odor mixtures.

The two independently estimated response kernels for each component odor (left, red and black) in the fluctuating binary mixture are overlaid for convenient comparison of relative amplitudes and temporal dynamics across the two component odors. Odors used are indicated above each kernel. Odors were delivered at 1% saturation. On the right, observed and predicted mean firing rate response of the two M/T cells to pseudo-random fluctuating patterns of the two component odors and to their fluctuating mixture combination are depicted. Predictions for individual odor responses were obtained using kernels shown on the left. Predictions for the fluctuating mixture combination were obtained by summing up the predicted response to each of the two individual odor stimulus patterns. **(c)** Estimated odor kernels (left) and observed and predicted firing rate responses (right) of two M/T cells to individual pulses of two odors presented independently, as well as in combination, at different temporal lags. The independently estimated response kernels for each component odor (left, red and black) in the fluctuating binary mixture are overlaid for convenient comparison of relative amplitudes and temporal dynamics across the two component odors. Odors used are indicated above each kernel. Both odors were delivered at 1% saturation. On the right, observed and predicted mean firing rate response of the two M/T cells to individual pulses of two odors presented independently, as well as in combination, at different temporal lags are depicted. Predictions for individual odor pulses were obtained using kernels shown on the left. Predictions for the stimuli in which both odors were presented were obtained by summing up the predicted response to each of the two individual odor pulses. **(d)** Summary plot showing comparison of the residual error between predicted and observed firing rates with the trial-to-trial variation (noise) in the observed response across all stimuli containing binary odor combinations. Each dot represents one stimulus pattern in a scatter plot of $\sqrt{\text{signal/residual}}$ against $\sqrt{\text{signal/noise}}$. Points lying above the slope of unity (dashed black line) indicate that deviation of the fit from the mean is less than the trial-to-trial variability in the response. 314 stimulus patterns, 48 M/T cell-mixture pairs. Red, yellow, cyan and brown circles correspond to the responses of the four example M/T cells shown in **b,c**. Marginal histograms show distribution of $\sqrt{\text{signal/noise}}$ (top) and $\sqrt{\text{signal/residual}}$ (right) across all cell-stimulus pairs. \pm indicate median and s.d. Left tail t -test, $P > 0.05$. **(e)** Summary histogram of r between the predicted and observed mean firing rate response for all cell-stimulus pairs containing binary odor combinations. \pm indicates median and s.d. **(f)** Summary histogram of fve by the model across all cell-stimulus pairs containing binary odor combinations. \pm indicates median and s.d. For **a-c**, vertical green bars indicate on periods for odor A; vertical tan bars indicate on periods for odor B; blue indicates periods when the two odors were presented simultaneously (binary mixture). For **b,c**, black lines show the observed mean firing rate response across 12 trials; gray bands mark s.e.m.; red lines show model predictions. M/T cells, $n = 47$; patterns, $n = 314$; odors, $n = 9$.

Figure 5 Linear summation predicts respiration tuning of M/T cell odor responses. **(a)** Schematic of the linear model for respiration. The odor-evoked change in firing rate of an M/T cell (blue) upon odor presentation (indicated by gray boxes) was calculated by convolving the odor kernel (estimated from odor responses in the tracheotomized rat) with the respiration waveform (measured via a pressure sensor in the free-breathing condition). For the convolution, the exhalation component (yellow shading) was discarded and only the inhalation component (green shading) of the respiration was used as a measure of the positive odor influx in the nose. The predicted odor-evoked change in firing rate (blue) was summed with the observed (measured) baseline respiration-tuned response of the M/T cell (black, air periods) and thresholded to discard negative firing rates to obtain the predicted respiration-tuned odor response of the M/T cell (red). **(b)** Estimated odor kernels (top) and comparison of the observed and predicted respiration-tuned odor response (bottom) of three M/T cells. Odor kernels were estimated for each M/T cell from responses to time-varying stimuli delivered when the animal was tracheotomized (top left schematic). Odors used are indicated above each kernel. Odors were delivered at 1% saturation (top). Baseline (air) and odor-evoked (odor on) respiration-tuned responses of the M/T cells measured after reconnecting the tracheal loop (middle left schematic). Respiration was measured using a pressure sensor connected in the tracheal loop. Respiration-tuned responses are shown as spike rasters and PSTHs across 12 respiration cycles each during the air period and the odor on period. Vertical lines in spike raster show individual spikes, plotted at 1-ms resolution. Black lines in the PSTH show mean firing rate across 12 cycles. Gray bands indicate s.e.m. The average pressure sensor waveforms (respiration) are shown in black above the spike rasters. Predicted respiration-tuned odor response (red lines) was calculated using the linear model described in **a**. **(c)** Summary histogram of r between the predicted and observed respiration-tuned odor response for all cell-odor pairs. \pm indicates median and s.d. Analysis includes only the first respiration cycle after odor onset. **(d)** Summary plot showing comparison of the residual error between predicted and observed respiration-tuned odor response with the trial-to-trial variation (noise) in the observed response across all cell-odor pairs. Each dot represents one cell-odor pair in a scatter plot of $\sqrt{\text{signal/residual}}$ against $\sqrt{\text{signal/noise}}$. Points lying above the slope of unity (dashed black line) indicate that deviation of the fit from the mean is less than the trial-to-trial variability in the response. Cell-odor pairs, $n = 43$; M/T cells, $n = 19$; odors, $n = 6$. Analysis includes only the first respiration cycle after odor onset.



concentrations. For example, the kernel at 2% concentration would be identical to the kernel at 1% concentration but doubled in amplitude.

For each concentration pair, we plotted the two kernels point by point against each other and used simple regression to calculate the best linear fit between the two kernels. This allowed us to assess changes in both overall kernel shape (correlation statistic (R^2)) and amplitude (slope of the regression line) for each pair of kernels (Fig. 3b). According to this metric, perfect linear scaling would be indicated by a slope as well as correlation coefficient of unity. M/T cell odor kernels in our data set (30 cell-odor pairs) showed both linear and nonlinear transitions in shape, as indicated by the wide distribution of correlation coefficients (Fig. 3c). Further, even when kernels remained similar in shape, responses did not scale linearly in proportion to the change in odor concentration (Fig. 3c). Although the amplitude scaling of the kernels at all concentrations was sublinear, the departure from similarity in kernel shape across concentrations was more pronounced at transitions between lower concentrations (0.4–1%) (Fig. 3c). Across higher concentrations (1–3.5%), the kernel shapes remained quite similar (Fig. 3c). Notably, despite sublinear scaling and changes in kernel shape, the linear model reliably predicted firing rate responses at each independent concentration (Fig. 3d–f).

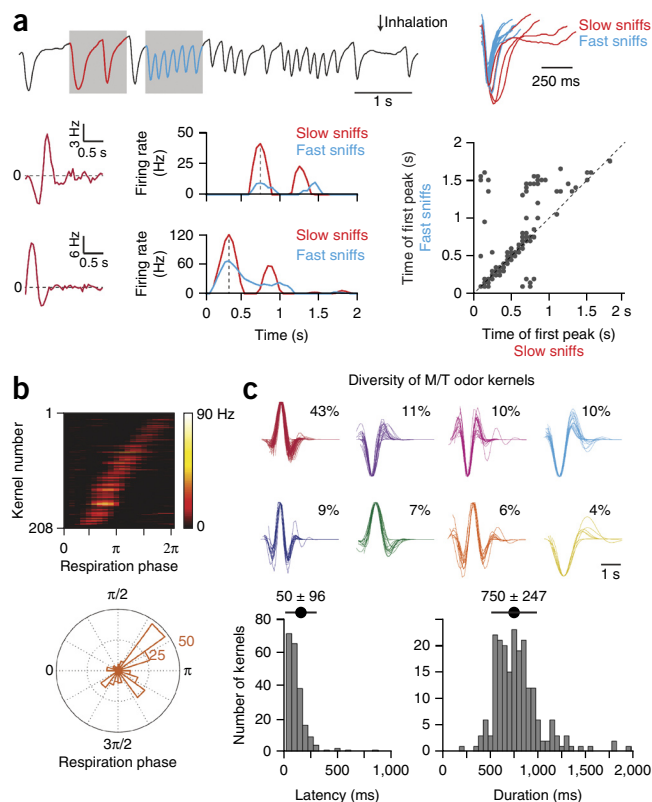
These results (Figs. 2 and 3) suggest that individual M/T cells integrate fluctuating inputs of a given odor linearly in time, across all sampled

concentrations, but the kernel shapes may change nonlinearly across concentrations (see Discussion).

Response to binary odor mixtures is the sum of components

We presented pseudo-random patterns³⁴ of two different odors simultaneously (Supplementary Fig. 5) to explore summation of both co-incident and temporally separated odor inputs (Fig. 4a). Summation of predicted responses to the individual odor patterns accurately accounted for the response to the superimposed presentation of the two odor patterns (Fig. 4b,c). Using pairs of pulses that overlap for different durations³⁰, we verified that summation of responses accounted for the observed response independent of the temporal overlap between the two odors (Fig. 4c). In 89% of cases (279 out of 314 stimuli), the prediction error was less than intertrial noise in the observed response (left tail t -test, $P > 0.05$, Fig. 4d and Supplementary Fig. 6a). Further, the correlation between the observed and predicted responses, as well as the stimulus-related variance

Figure 6 Model predictions of M/T cell response properties and kernel diversity. **(a)** Model predictions of M/T cell response latency during slow and fast sniffing. Top left, sniff waveforms recorded in awake, behaving rats. Data adapted from Cury *et al.*³⁷. Red and blue traces indicate periods of slow (~2 Hz) and fast (~7 Hz) sniffing that were used for calculating response latencies in bottom middle and bottom right graphs. Gray boxes indicate odor presentation (top left image of **a** reproduced with permission from ref. 41). Top right, stereotypy in inhalation onset dynamics of individuals sniffs from the sniff waveforms shown in top left image. Sniffs were aligned by time of inhalation onset. Bottom left, example odor kernels of two M/T cells. Bottom middle, response of the M/T cells in bottom left graphs during slow sniffing (red) and fast sniffing (blue), predicted by convolution of the kernels with the respiration waveforms in top left image. Dashed lines indicate the first peak in firing rate after inhalation onset. Bottom right, comparison of response latencies of predicted M/T cell odor responses during slow and fast sniffing. Each dot represents the ratio of predicted response latency at ~7 Hz and ~2 Hz for a given odor kernel ($n = 208$). Most dots lie on the black line, which indicates a ratio of unity. **(b)** Predicted M/T cell firing phase responses tile the full respiration cycle. Top, color map showing preferred respiration phase of M/T cell firing across all recorded M/T cells. Each row represents predicted odor-driven, respiration-tuned response for a given odor kernel ($n = 208$). Color indicates the firing rate. Responses are sorted (bottom to top) in increasing order of preferred firing phase from inhalation onset. The x axis represents one respiration cycle (duration 1 s) beginning with inhalation, binned uniformly into 20 phase bins. Color indicates instantaneous firing rate in hertz. Bottom, circular histogram of preferred phases of predicted M/T cell odor responses shown in top image. Dotted concentric circles indicate intervals of 25 M/T cells. **(c)** Diversity of M/T cell odor kernels. Top, classification of parameterized M/T cell odor kernels into eight distinct families via hierarchical clustering. Colors show the individual kernels within each family. Kernels are aligned by time of peak response and normalized by the peak amplitude. Relative abundance of each type is indicated as percentage of all kernels. Bottom left, histogram of response latency of the parameterized odor kernels. \pm indicates median and s.d. Bottom right, histogram of response duration of the parameterized odor kernels. \pm indicates median and s.d.



explained by the model, remained high across all cell-mixture pairs (Fig. 4e,f and Supplementary Fig. 6b), even when the kernels for the two odors composing the mixture were different in temporal dynamics (Supplementary Fig. 6c–e).

Taken together, these results (Figs. 2 and 4) support linear encoding of time-varying inputs of individual odors and their binary odor combinations across both inhibitory and excitatory responses.

Linear transform of odor inputs predicts respiration tuning

We next asked if kernels estimated in the tracheotomized animal could predict the odor-evoked response during respiration-modulated sampling (Fig. 5a). We recorded odor responses of individual M/T cells during both tracheotomized and free-breathing conditions (Fig. 5b and Online Methods). We predicted the odor-evoked change in firing rate of a cell by convolving the estimated kernel (from responses in the tracheotomized rat; Fig. 5b) with the average ‘inhalation’ waveform measured using a pressure sensor (Online Methods). To this predicted response, we added the average respiration-tuned baseline firing of the cell, measured from the respiration cycles preceding odor presentation (air periods) (Fig. 5a and Online Methods). The resulting outcome accurately captured the strength as well as the respiration-locked timing of both odor-evoked excitation and inhibition across multiple respiration cycles (Fig. 5b). For quantification, we considered only the first respiration cycle after odor onset because it was best aligned to odor delivery.

The model predictions showed high correlation with the observed respiration tuning (Fig. 5c) and matched the respiration tuning within noise limits of intercycle variability (residual < noise, 28 out of 43 cell-odor pairs, left tail t -test, $P > 0.05$; residual = noise, 14 out of

43 cell-odor pairs, two-sided t -test, $P > 0.05$) (Fig. 5d). These results represent the lower boundary of the model’s predictive power, given two factors that reduce the model’s predictive power: (i) poor knowledge of underlying inhibition strength in the baseline respiration tuned response (zero firing periods) and (ii) use of pressure sensor output as a proxy for nasal odor concentration.

Thus, the well-known respiration tuning of odor responses emerges from and is predicted by the convolution of odor impulse responses with the respiratory cycle.

Linear model predicts key temporal aspects of M/T cell responses

We next tested whether the model explains other M/T cell response properties reported previously in awake, freely breathing rodents. Specifically, we focused on two recent findings: (i) sniff frequency-invariant latency of M/T cell responses³⁷ in awake, behaving rats and (ii) tiling of respiration cycle by M/T cell odor responses³⁸ in awake, head-fixed mice.

We calculated the latency of M/T cell responses at various sniff frequencies by convolving the kernels in our data set with canonical sniff waveforms recorded by Cury *et al.*³⁷ during slow (~2 Hz) and fast (~7 Hz) sniffing (Fig. 6a). Consistent with Cury *et al.*³⁷, we found that the response latency of a given M/T cell was largely unaffected by sniff frequency (Fig. 6a). Several studies have proposed a latency code for odor identity in the olfactory system. Different odor-specific latencies across M/T cells emerged from diversity in kernel shapes both across odors and cells (Fig. 6a). Interestingly, our results suggest that sniff-frequency invariance of M/T cell response latency may not require specialized circuit mechanisms and instead simply result from stereotypy in inhalation onset time courses (similar slope) across

various sniff frequencies, despite differences in amplitude and duration of individual sniffs (Fig. 6a; also see sniff waveforms reported in refs. 39,40).

We analyzed the tiling of the respiration cycle by sorting the predicted respiration-tuned responses of all kernels by their preferred phase of firing in the respiration cycle. This revealed a broad distribution of preferred respiration phases that spanned both inhalation and exhalation, with a bias toward inhalation, similar to that reported by Shusterman *et al.*³⁸ (Fig. 6b). Systematic characterization of the kernel diversity using parametric analysis and hierarchical clustering revealed 8 distinct families (Fig. 6c). Kernels within each family differed only in overall amplitude but had similar time courses. On average, we found 64% primarily excitatory and 36% primarily inhibitory kernels with a median response latency of 50 ± 96 ms and average duration of 750 ± 247 ms (Fig. 6c).

Our observations suggest that the broad distribution of M/T cell firing across the respiratory cycle, with sniff-frequency invariant response latencies, results from the linear convolution of diverse M/T cell odor kernels with stereotypic inhalation onset dynamics.

DISCUSSION

We used precisely controlled, time-varying odor stimuli and respiration-decoupled odor sampling to characterize M/T cell responses to fluctuating inputs of individual odors and their binary mixtures (Fig. 1). We found that individual M/T cells linearly sum inputs of a given odor across time (Figs. 2 and 3). Responses to binary mixtures reliably matched the sum of responses to the individual odors (Fig. 4). Using reversible tracheotomy, we showed that respiratory patterning and sniff-frequency invariant latency of M/T cell firing are emergent properties of linear summation, diverse M/T cell response kernels and respiratory cycling (Figs. 5 and 6).

Comparison with previous work

Our results are in contrast with previously reported nonlinear summation properties of M/T cell homologs in the locust and zebrafish olfactory systems^{30,31,34}. The differences in results may originate from distinct network architectures between mammals, fish and insects¹³, as well as methodological differences in stimulus control. Two recent studies that have applied carefully controlled odor delivery methods, albeit in a different model system (fruit fly ORNs), have reported linear integration of odor inputs by the ORNs^{28,29}. Prediction failures in some studies may also be attributed to use of time-invariant stimuli that do not allow accurate estimation of the strength of inhibitory responses.

We stress that tight control of stimulus conditions was necessary to observe linear summation of responses. These conditions included the lack of flow transients during air-odor transitions, reproducibility of odor amplitude and time course, and rapid kinetics to prevent odor spillover between consecutive pulses. In our experience, deviation from this tightly controlled stimulus regime along with anesthesia-related instability in recordings resulted in substantial degradation of linearity. Although a few elegant odor delivery systems have been described recently for precise control of odor concentration of individual odors^{28,29}, the odor delivery system used in this study is a low-cost, integrated solution for interleaved presentation of deterministic, arbitrary time waveforms of individual odors, mixtures and concentrations at fast time scales (20 Hz). It is ideally suited for future behavioral experiments that require interleaved presentations of multiple odors (or concentrations) and rely on careful concentration control while mimicking natural stimulus dynamics.

A biophysical basis for bulbar linearity

M/T cells receive direct excitatory input from a principal parent glomerulus and lateral excitatory and/or inhibitory inputs from other glomeruli via local interneurons. This circuit is highly nonlinear: both the odorant receptor response properties^{41,42} and the responses of individual M/T cells^{16,22,23} are nonlinear. In principle, the cross-coupling of glomeruli through local inhibitory networks could simply shut off mitral cells, which is a rectifying nonlinearity.

Linearity may nevertheless emerge from a more nuanced analysis of bulbar network experiments and network theory. Mitral cells show activity-dependent cross-inhibition⁴³. This implies that inhibitory effects from other glomeruli are not binary shutdown operations but activity modulations. Furthermore, the structure of the inhibitory network introduces negative feedback onto M/T cells through reciprocal dendro-dendritic synapses, both through juxtglomerular and granule cells¹³. Negative feedback is the classic electronic circuit motif for linearizing otherwise nonlinear network responses⁴⁴.

Intrinsic factors such as response adaptation and saturation of neuronal firing could also in principle trigger nonlinear outcomes. Interestingly, we found that commonly reported 'nonlinear' temporal adaptation of M/T cell responses to strong, sustained inputs was well captured by linear processing, given the presence of both excitatory and inhibitory components in individual M/T cell kernels. For example, the strength of odor-evoked excitation, as well as inhibition (Fig. 2c), often decayed systematically across time for odor pulses lasting up to 2 s. However, this response decay was accounted for by the inhibitory period in the M/T cell kernel following excitation for cell no. 96 (Fig. 2b) and conversely by the excitatory bump following odor-evoked inhibition for cell no. 104 (Fig. 2b). The same mechanism may prevent M/T cells from reaching their maximal (saturating) firing rates, explaining the lack of saturation-related nonlinearities in our data set.

At the single-cell level, we predict that the summation of inhibitory and excitatory currents on M/T cells directly maps onto the summation of negative and positive regions of response kernels in our model. This is consistent with the overlap of predicted 'negative firing rates' with periods of experimentally observed zero spiking, indicating the presence of underlying inhibitory currents. We propose that the kernel shape itself is determined by the summed contribution of all glomeruli (connected to the M/T cell) activated by the odor at any particular concentration. Future experiments using optogenetic mapping¹⁷ of the glomerular receptive field of M/T cells coupled with intracellular recordings from M/T cells will allow direct testing of this hypothesis.

Implications of nonlinear concentration dependence

We found that M/T cells linearly integrate inputs of a given odor across time, at both low (0.5% saturation) and high (3.5% saturation) extremes of the tested concentration range. However, kernel dynamics varied nonlinearly across concentrations (Fig. 3c). We suggest that this deviation from linearity arises because different glomeruli differ in their sensitivity to a given odor. With increasing odor concentration the glomerular activity map changes both spatially and temporally^{8-10,12}: the additional odor-responsive glomeruli modulate the responses of mitral cells through the bulbar network, thus altering their response kernels. However, given the overall high sensitivity of olfactory receptors, recruitment of new glomeruli is more likely when concentrations jump from low to mid-range (from 0.4% to 1% in our study), as indicated by more frequent nonlinear alterations in kernel shape within this concentration range (Fig. 3c). At higher concentrations, the recruited glomerular pattern is relatively stable,

but responses of individual glomeruli may saturate, mostly resulting in sublinear scaling of kernel amplitudes with less impact on the overall kernel shape (Fig. 3c).

How do responses to odor mixtures remain linear, given that presentation of multiple odors would in principle recruit additional glomeruli? We suggest that linearity of responses to mixtures is maintained because of the sparse nature of glomerular odor representations^{11,45}, which results in little overlap between sets of activated glomeruli in mixtures. In situations in which the glomerular overlap between the two odors is high, or in the extreme case when the two components are identical (same odor added to itself equals higher concentration of a given odor), the summation of observed responses would not remain linear.

How is linearity maintained for any time-varying stimulus given that the odor concentration swings between zero and a set peak value? Should not these concentration excursions also introduce nonlinearities? Given the fast kinetics of our odor delivery system, the concentration transitions to within 80% of the peak value in <40 ms. Intermediate concentrations thus constitute only a small fraction of the total 'on' stimulus time. Fast time-scale changes in odor concentration are typical of both natural odor plume statistics and inhalation-dependent odor sampling, suggesting that simple linear integration may well apply under naturalistic conditions. This is consistent with the accurate model predictions of both amplitude and time-course of responses in free-breathing rats in our study, despite different nasal flow rate conditions in the tracheotomized versus free-breathing state.

There still remains the question of how animals identify an odor across discrete encounters at widely different concentrations, such as are commonly encountered in nature. Our data rule out the simplest model for odor identification, in which only a single kernel per odor per cell is needed, provided it scales linearly with concentration. The slightly less general model, in which a single kernel scales nonlinearly, accounts for a few but not all cases. Instead, we propose that odor recognition requires knowledge of a concentration profile of kernels for each odor. One possibility is that the olfactory system extracts odor identity by learned mapping of multiple impulse response functions to a given odor on the basis of previously encountered concentrations through local processing in the cortex or via feedback to the olfactory bulb. This is consistent with observations of perceptual discontinuity in odor recognition at extreme concentrations. Another possibility is that pooling multiple M/T cells onto cortical neurons averages out cell-specific dependencies on odor concentration, yielding a concentration-invariant impulse response for the pooled population. Similar mechanisms for concentration-invariant decoding of odor identity have been proposed in the invertebrate olfactory system^{32,33,46}. Future work combining behavior and circuit analysis will help disambiguate these possibilities and establish a complete model for decoding stimulus identity, intensity and timing in the olfactory system.

Together our results imply that a complete model of bulb input-output transform requires knowledge of the concentration-profile of response kernels in addition to the basic mechanism of linear summation. Nonlinearities in responses are inevitable for any sensory circuit given the intrinsic nature of neuronal firing (action potentials) and the mismatch between the range of stimulus intensities and that of neuronal firing rates. The striking aspect of our findings is that despite these factors, M/T cell responses are linear across a wide range of temporal variations in odor stimuli (tracheotomized as well as free breathing) and their binary combinations. It is important to emphasize that the proposed linear model is in no manner complete, and it needs to be further tested in awake animals in which context-dependent brain

states play substantial roles in shaping the response properties of M/T cells. Nevertheless, this minimal framework captures a wide spectrum of fundamental response features of the olfactory bulb, accounting for the classical sniff-locked firing of OB neurons and the diversity in responses to odor mixtures and transients in odor plumes.

Insights from the model: how respiration aids bulbar coding

Since the first recordings in the mammalian olfactory system, M/T cell odor responses have been shown to be time locked to respiration^{14,15}. Given that respiratory sampling is the 'natural' condition, there has been relatively little interest in more artificial airflow protocols. However, respiration frequencies vary over a wide range, so this 'natural' condition is hardly singular. We argue that the basic circuit response is defined by, and best studied in terms of, impulse responses. Below we consider cases in which this point of view may offer some insights.

Respiration tuning from odor-specific impulse responses, invariant of the sniff frequency. The diverse repertoire of M/T cell respiratory tuning^{17,38} can be predicted as an emergent outcome of M/T cell impulse responses (kernels) convolved with respiration-modulated odor influx through fast or slow sniffs. Our model predicts that response latency of M/T cells is odor specific and invariant of the sniff frequency, providing a substrate for temporal encoding of odor identity in the M/T cell response latencies. Interestingly, we find that the invariance of response latency to sniff frequency results from strikingly conserved dynamics of inhalation onsets across fast and slow sniffs. We propose that the olfactory system utilizes stereotypy in inhalation dynamics in conjunction with respiratory cycling of diverse M/T cell kernels to facilitate latency coding of odor identity, invariant of changes in sniff patterns.

Intermittent inputs improve system performance. Analytical studies have suggested that the spatiotemporal structure of plumes may encode source-related information^{47,48}. Though stimulus intermittency has been demonstrated to be behaviorally relevant for odor tracking^{2,49,50}, it remains unclear how the olfactory system evaluates odor plume statistics. In our analysis, the 'inhibitory' components of the response kernels were unmasked only in response to rapidly fluctuating stimuli. In steady state, these inhibitory components lead to zero firing. When the stimulus fluctuates, the excitatory and inhibitory components overlap, and the subtleties of the inhibitory components are unmasked as modulations of the excitatory components. Thus, from the viewpoint of our model, the olfactory system can linearly decode the contributions of the dense inhibition in the network precisely because of the intermittent nature of inputs. Along the same lines, we suggest that the respiratory cycle, far from being a sampling constraint on olfaction, improves sensitivity and discrimination by introducing natural pulsatile sampling. Although it is challenging to externally modulate sniff rates in the awake animal, optogenetic stimulation of glomeruli at different temporal frequencies during behavior may allow analysis of odor identification acuity as a function of stimulus intermittency.

Our findings provide a concise framework for the input-output function of the olfactory bulb, explaining most of the variance in the bulb responses. We propose that, at the single-neuron level, a major computational function of the olfactory bulb is to linearize signals and convolve them in time with a palette of odor-specific impulse-response functions. This raises interest in further understanding how this linear transform is achieved given the complexity of local microcircuits in the bulb and feedback from other brain areas.

Furthermore, these results provide a simple mathematical abstraction of the bulb inputs to the olfactory cortex, opening new avenues for studying downstream processing of olfactory information.

METHODS

Methods and any associated references are available in the [online version of the paper](#).

Note: Supplementary information is available in the [online version of the paper](#).

ACKNOWLEDGMENTS

We would like to thank M. Thattai, A.K. Dhawale, A.G. Khan, A. Gilra, G.H. Otazu, M. Kaufman and K. Parthasarathy for valuable inputs on experiment design, data analysis and manuscript preparation, and V.N. Murthy, R. Rajan, R. Campbell, F. Anselmi, A. Banerjee, M. Koh, U. Livneh, B. Hangya and members of the Bhalla and Albeanu laboratories for comments on the manuscript. This study was supported by a grant from the Department of Biotechnology, India, a Whitehall Foundation fellowship, a Committee for Aid and Education in Neurochemistry fellowship and Cold Spring Harbor Laboratory and National Centre for Biological Sciences funds.

AUTHOR CONTRIBUTIONS

P.G. and U.S.B. conceptualized the study. All authors contributed to the practical design of experiments and analysis. P.G. performed the experiments and analyzed the data. P.G., D.F.A. and U.S.B. wrote the manuscript.

COMPETING FINANCIAL INTERESTS

The authors declare no competing financial interests.

Reprints and permissions information is available online at <http://www.nature.com/reprints/index.html>.

1. Crimaldi, J.P., Wiley, M.B. & Koseff, J.R. The relationship between mean and instantaneous structure in turbulent passive scalar plumes. *J. Turbul.* **3**, 014 (2002).
2. Vickers, N.J. Mechanisms of animal navigation in odor plumes. *Biol. Bull.* **198**, 203–212 (2000).
3. Koehl, M.A.R. The fluid mechanics of arthropod sniffing in turbulent odor plumes. *Chem. Senses* **31**, 93–105 (2006).
4. Wallace, D.G., Gorny, B. & Whishaw, I.Q. Rats can track odors, other rats, and themselves: implications for the study of spatial behavior. *Behav. Brain Res.* **131**, 185–192 (2002).
5. Uchida, N. & Mainen, Z.F. Speed and accuracy of olfactory discrimination in the rat. *Nat. Neurosci.* **6**, 1224–1229 (2003).
6. Rajan, R., Clement, J.P. & Bhalla, U.S. Rats smell in stereo. *Science* **311**, 666–670 (2006).
7. Khan, A.G., Sarangi, M. & Bhalla, U.S. Rats track odour trails accurately using a multi-layered strategy with near-optimal sampling. *Nat. Commun.* **3**, 703 (2012).
8. Rubin, B.D. & Katz, L.C. Optical imaging of odorant representations in the mammalian olfactory bulb. *Neuron* **23**, 499–511 (1999).
9. Meister, M. & Bonhoeffer, T. Tuning and topography in an odor map on the rat olfactory bulb. *J. Neurosci.* **21**, 1351–1360 (2001).
10. Spors, H. & Grinvald, A. Spatio-temporal dynamics of odor representations in the mammalian olfactory bulb. *Neuron* **34**, 301–315 (2002).
11. Soucy, E.R., Albeanu, D.F., Fantana, A.L., Murthy, V.N. & Meister, M. Precision and diversity in an odor map on the olfactory bulb. *Nat. Neurosci.* **12**, 210–220 (2009).
12. Fletcher, M.L. *et al.* Optical imaging of postsynaptic odor representation in the glomerular layer of the mouse olfactory bulb. *J. Neurophysiol.* **102**, 817–830 (2009).
13. Wilson, R.I. & Mainen, Z.F. Early events in olfactory processing. *Annu. Rev. Neurosci.* **29**, 163–201 (2006).
14. Adrian, E.D. Olfactory reactions in the brain of the hedgehog. *J. Physiol. (Lond.)* **100**, 459–473 (1942).
15. Macrides, F. & Chorover, S.L. Olfactory bulb units: activity correlated with inhalation cycles and odor quality. *Science* **175**, 84–87 (1972).
16. Khan, A.G., Thattai, M. & Bhalla, U.S. Odor representations in the rat olfactory bulb change smoothly with morphing stimuli. *Neuron* **57**, 571–585 (2008).
17. Dhawale, A.K., Hagiwara, A., Bhalla, U.S., Murthy, V.N. & Albeanu, D.F. Non-redundant odor coding by sister mitral cells revealed by light addressable glomeruli in the mouse. *Nat. Neurosci.* **13**, 1404–1412 (2010).
18. Fukunaga, I., Berning, M., Kollo, M., Schmaltz, A. & Schaefer, A.T. Two distinct channels of olfactory bulb output. *Neuron* **75**, 320–329 (2012).
19. Junek, S., Kludt, E., Wolf, F. & Schild, D. Olfactory coding with patterns of response latencies. *Neuron* **67**, 872–884 (2010).
20. Schaefer, A.T. & Margrie, T.W. Spatiotemporal representations in the olfactory system. *Trends Neurosci.* **30**, 92–100 (2007).
21. Laurent, G. *et al.* Odor encoding as an active, dynamical process: experiments, computation, and theory. *Annu. Rev. Neurosci.* **24**, 263–297 (2001).
22. Chalansonnet, M. & Chaput, M.A. Olfactory bulb output cell temporal response patterns to increasing odor concentrations in freely breathing rats. *Chem. Senses* **23**, 1–9 (1998).
23. Giraudet, P., Berthommier, F. & Chaput, M. Mitral cell temporal response patterns evoked by odor mixtures in the rat olfactory bulb. *J. Neurophysiol.* **88**, 829–838 (2002).
24. Lin, D.Y., Shea, S.D. & Katz, L.C. Representation of natural stimuli in the rodent main olfactory bulb. *Neuron* **50**, 937–949 (2006).
25. McNamara, A.M., Magidson, P.D. & Linstor, C. Binary mixture perception is affected by concentration of odor components. *Behav. Neurosci.* **121**, 1132–1136 (2007).
26. Frederick, D.E., Barlas, L., Ivins, A. & Kay, L.M. A critical test of the overlap hypothesis for odor mixture perception. *Behav. Neurosci.* **123**, 430–437 (2009).
27. Vetter, R.S., Sage, A.E., Justus, K.A., Cardé, R.T. & Galizia, C.G. Temporal integrity of an airborne odor stimulus is greatly affected by physical aspects of the odor delivery system. *Chem. Senses* **31**, 359–369 (2006).
28. Kim, A.J., Lazar, A.A. & Slutskiy, Y.B. System identification of *Drosophila* olfactory sensory neurons. *J. Comput. Neurosci.* **30**, 143–161 (2011).
29. Martelli, C., Carlson, J.R. & Emonet, T. Intensity invariant dynamics and odor-specific latencies in olfactory receptor neuron response. *J. Neurosci.* **33**, 6285–6297 (2013).
30. Broome, B.M., Jayaraman, V. & Laurent, G. Encoding and decoding of overlapping odor sequences. *Neuron* **51**, 467–482 (2006).
31. Niessing, J. & Friedrich, R.W. Olfactory pattern classification by discrete neuronal network states. *Nature* **465**, 47–52 (2010).
32. Brown, S.L., Joseph, J. & Stopfer, M. Encoding a temporally structured stimulus with a temporally structured neural representation. *Nat. Neurosci.* **8**, 1568–1576 (2005).
33. Stopfer, M., Jayaraman, V. & Laurent, G. Intensity versus identity coding in an olfactory system. *Neuron* **39**, 991–1004 (2003).
34. Geffen, M.N., Broome, B.M., Laurent, G. & Meister, M. Neural encoding of rapidly fluctuating odors. *Neuron* **61**, 570–586 (2009).
35. Grosmaître, X., Santarelli, L.C., Tan, J., Luo, M. & Ma, M. Dual functions of mammalian olfactory sensory neurons as odor detectors and mechanical sensors. *Nat. Neurosci.* **10**, 348–354 (2007).
36. Sobel, E.C. & Tank, D.W. Timing of odor stimulation does not alter patterning of olfactory bulb unit activity in freely breathing rats. *J. Neurophysiol.* **69**, 1331–1337 (1993).
37. Cury, K.M. & Uchida, N. Robust odor coding via inhalation-coupled transient activity in the mammalian olfactory bulb. *Neuron* **68**, 570–585 (2010).
38. Shusterman, R., Smear, M.C., Koulakov, A.A. & Rinberg, D. Precise olfactory responses tile the sniff cycle. *Nat. Neurosci.* **14**, 1039–1044 (2011).
39. Verhagen, J.V., Wesson, D.W., Netoff, T.L., White, J.A. & Wachowiak, M. Sniffing controls an adaptive filter of sensory input to the olfactory bulb. *Nat. Neurosci.* **10**, 631–639 (2007).
40. Carey, R.M. & Wachowiak, M. Effect of sniffing on the temporal structure of mitral/tufted cell output from the olfactory bulb. *J. Neurosci.* **31**, 10615–10626 (2011).
41. Rospars, J.P., Lánský, P., Duchamp-Viret, P. & Duchamp, A. Spiking frequency versus odorant concentration in olfactory receptor neurons. *Biosystems* **58**, 133–141 (2000).
42. Duchamp-Viret, P., Duchamp, A. & Chaput, M.A. Single olfactory sensory neurons simultaneously integrate the components of an odour mixture. *Eur. J. Neurosci.* **18**, 2690–2696 (2003).
43. Arevian, A.C., Kapoor, V. & Urban, N.N. Activity-dependent gating of lateral inhibition in the mouse olfactory bulb. *Nat. Neurosci.* **11**, 80–87 (2008).
44. Horowitz, P. & Hill, W. *The Art of Electronics* (Cambridge University Press, 1989).
45. Fantana, A.L., Soucy, E.R. & Meister, M. Rat olfactory bulb mitral cells receive sparse glomerular inputs. *Neuron* **59**, 802–814 (2008).
46. Broome, B.M., Jayaraman, V. & Laurent, G. Encoding and decoding of overlapping odor sequences. *Neuron* **51**, 467–482 (2006).
47. Murlis, J., Elkinton, J.S. & Cardé, R.T. Odor plumes and how insects use them. *Annu. Rev. Entomol.* **37**, 505–532 (1992).
48. Hopfield, J.J. Olfactory computation and object perception. *Proc. Natl. Acad. Sci. USA* **88**, 6462–6466 (1991).
49. Webster, D.R. & Weissburg, M.J. Chemosensory guidance cues in a turbulent chemical odor plume. *Limnol. Oceanogr.* **46**, 1034–1047 (2001).
50. Willis, M.A., Avondet, J.L. & Finnell, A.S. Effects of altering flow and odor information on plume tracking behavior in walking cockroaches, *Periplaneta americana* (L.). *J. Exp. Biol.* **211**, 2317–2326 (2008).

ONLINE METHODS

Odor stimuli. Odor stimuli were delivered via a custom-designed odor delivery system (Fig. 1a) optimized for reproducible and fast stimulus kinetics and absence of pressure transients associated with stimulus presentation (Supplementary Fig. 1).

Basic design of the odor machine. To achieve linear odor output, we used nitrogen-borne or airborne saturated odor streams diluted serially by clean air. The input rate into the odor vials was regulated at 0.5 l/min using acrylic block flow meters (EW-32460-40, Cole-Parmer). Two independently controllable channels were used to deliver binary odor combinations in any desired overlapping or non-overlapping temporal sequences. In each channel, saturated odor vapor was produced by bubbling the carrier nitrogen (or air) stream through a glass vial containing undiluted, liquid odor (Fig. 1a). Odor selection was done using a digitally controlled solenoid valve assembly that channeled the stream through any one of four odor vials at a time (Fig. 1a). Glass beads were immersed in the odor to aid saturation and prevent aerosol formation. The saturated vapor was brought to 10% dilution by mixing with a 5 l/min stream of charcoal filtered and dehumidified air. Only 0.5 l/min of this odorized stream was directed further to the final manifold; the rest was ejected through the exhaust (Fig. 1a). One-way check valves were used to prevent backflow of the diluting air stream into the odor vial. The final manifold was a custom-designed assembly of four input channels, each of which bifurcated into two output channels gated by four pairs of digitally controlled solenoid valves (ET-2M-12, Clippard) mounted on the manifold. One of the output channels was directed to the rat and the other to the exhaust (Fig. 1a). Simultaneous switching of the diluted odor streams between valves gating the rat and the exhaust channel allowed rapid turning on and off of odor without introducing backpressure in the system (reduced flow transients). Further, for each odor stream, we used a flow-rate-matched clean air stream that also switched between rat and exhaust in a complementary fashion to keep the net output flow rate of the channels unchanged. To further minimize the pressure transient at the switch, the input flow rate of the four streams at the manifold was kept low and fixed at 0.5 l/min. The output channels were flushed continuously with a high-flow-rate stream (5 l/min) of clean humidified air, thus leading to a second, tenfold dilution of the odor.

The two-step serial dilution design reduces pressure transients and gives fast switching as follows. Low flow rate of the odor stream at the switching point minimizes any pressure transients as the odor valve is turned on or off. This is important to avoid mechanosensory M/T cell responses³⁵. The subsequent dilution with a high-flow-rate air stream allows for rapid odor clearance, thus accelerating stimulus kinetics. To further enhance the kinetics, we used short-length (<10 cm), narrow-diameter tubing (4 mm) at the exit port, kept a small distance (~1 cm) outside the animal's snout.

Modified design of the odor machine for linear and interleaved concentration control. We adapted the above-described design to deliver three different concentrations of a selected odor within the range of 0.4–3.5% saturation to meet three primary conditions.

(i) Maintaining the same relative difference across the three concentrations irrespective of the chemical nature of the selected odor. Typically, increasing odor concentrations are obtained by flushing increasing flow rates through the odor vial. We found that the range of concentrations produced by this approach was highly dependent on odor chemistry and often resulted in unexpectedly supra-linear odor output at lower flow rates for viscous odors. We bypassed this limitation by using only one saturation step (flow through the odor vial) for each odor and distributing the saturated odor stream into different concentration banks (dilution 1, dilution 2, etc.; Supplementary Fig. 4a) by multiple serial dilutions. As a result, the relative difference between the outputs of different concentration banks was purely dictated by the dilution factor and did not depend on individual odor chemistry (Supplementary Fig. 4b–c).

(ii) Interleaving presentations of different concentrations in quick succession, with no cross-contamination between concentrations. To this end, we exploited our original design for delivery of odor mixtures and treated the output of each concentration bank as an independent odor, using a dedicated set of solenoid valves for each bank. Thus, a low-concentration trial could be presented immediately following a high-concentration trial with no spillover of odor from the previous trial. This can be appreciated in the low intertrial variability of the observed PID responses for different concentration trials, even when all concentrations were presented in a randomly interleaved sequence (Supplementary Fig. 4b–c).

(iii) Achieving low variability in the absolute odor concentration. Because our analysis was aimed at quantifying changes in M/T responses as a function of odor strength, it was critical for us to reliably maintain the absolute odor concentration throughout the recording duration for a given cell (~1.5 h). We found that depending on the volatility of different odors, the concentration may drop to half its original amplitude within 30 min of continuous usage (e.g., ethyl butyrate). However, replenishing the odor volume to match the initial amount in the vial immediately restored the PID readings to their original values. We therefore independently characterized the decay in odor concentration for each odor and replenished odor volumes in the vial at the appropriate frequency for each odor (ethyl butyrate, every 15 min; ethyl tiglate, every 30 min). This can be appreciated in the low variability across individual trials in the example PID responses in Supplementary Figure 4c. The individual trials (gray lines) for each concentration are randomly interspersed across a duration of 1.5–2 h.

Additionally, for the higher concentrations, care was taken to replace the valves periodically as the high concentration odors frequently clogged both the solenoid and check valves. For the same reason, we restricted the highest concentration tested in our experiments to 3.5%. At concentrations >3.5%, valves could be clogged even within one recording session, making the measured M/T cells responses unreliable.

Odors used. We used a total of nine odors: isoamyl acetate (W205532, Sigma-Aldrich), 1,4-cineole (W365807, Sigma-Aldrich), limonene (W504505, Sigma-Aldrich), methyl amyl ketone (W254401, Sigma-Aldrich), amyl acetate (W504009, Sigma-Aldrich), ethyl tiglate (W246018, Sigma-Aldrich), γ -terpinene (W355909, Sigma-Aldrich), linalool (W263508, Sigma-Aldrich) and ethyl butyrate (W242705, Sigma-Aldrich). The odors were chosen on the basis of detectable PID signals and rapid clearance from the solenoid valves and tubing while maintaining a diverse range of functional groups in our odor stimulus panel. Odors like 1-octanol, 1-hexanol, citral, etc., that did not evoke reproducible PID responses were excluded from the panel.

Stimulus patterns. We used a wide range of stimulus patterns to exhaustively characterize M/T responses to time-varying odor patterns: (i) individual pulses of variable duration (50, 100, 200, 500, 1,000 or 2,000 ms), (ii) non-overlapping pulse pairs of one or two odors (200 ms each) with variable interpulse duration (50, 100, 200, 500 or 1,000 ms), (iii) overlapping pulse pairs³⁰ of two odors (500 ms each) with variable interpulse overlap duration (0, 100, 200, 300, 400 or 500 ms), (iv) pulse trains with variable frequency (5, 10 or 20 Hz; duration 2 s), or (v) pseudo-random fluctuating pulse trains³⁴ (duration 5 s). The temporal pattern of odor valve opening and closing was described as string of 100 bits, in which each bit defined the binary on/off state of the valve in a 50-ms time period. Each bit was randomly assigned a value of 1 (on) or 0 (off) with equal probability. The minimum duration of an odor pulse was determined by the size of the smallest bin (50 ms). The maximum pulse duration was determined by the number of contiguous bits that were assigned the value of 1. We imposed an upper bound of 500 ms (10 bins) on this maximum by overriding the value of every 11th bin to be 0.

Stimulus characterization. We characterized the output stimulus concentration as a function of odor valve on/off state using a PID²⁷ (200B miniPID, Aurora scientific) placed at the odor machine outlet. Consistency of flow rate was measured using an anemometer (490-IS, Kurz Instruments) inserted in the path of the output flow 2 cm from the outlet. To characterize the kinetics (Supplementary Fig. 1a,b), we used 500-ms-long odor pulses and calculated the mean odor amplitude in the latter half of the valve on period (20 repeats per odor). We defined the on kinetics as the time taken to rise from 20% to 80% of the mean odor amplitude after valve opening. The average on kinetics was 40.1 ± 2.8 ms. The OFF kinetics was conversely defined as time taken to fall from 80% to 20% of the mean amplitude post valve closing. Additionally, we also calculated the dead time or the fixed delay to reach 20% mean odor amplitude from valve opening. This was found to be consistent across odors (31.6 ± 1.4 ms, Supplementary Fig. 1b). To characterize output linearity (Supplementary Fig. 4b), we measured the mean odor amplitude for 500-ms-long odor pulses (12 repeats) from randomly interleaved presentations of three different concentrations of each odor.

Reversible double tracheotomy and olfactory bulb exposure for extracellular single-unit recordings. We used standard methods described previously¹⁶ to record extracellular single-unit activity from the mitral cell layer in the olfactory bulb of tracheotomized, anesthetized female Wistar rats (250–350 g, 2–6 months old).

Briefly, animals were anesthetized with transient exposure to halothane followed by intraperitoneal administration of a ketamine (100 mg/kg) and xylazine (10 mg/kg) mixture. Pentathiol supplements (0.25 ml, 20%) at ~1-h intervals were used to maintain a stable anesthesia plane (respiratory rhythm of ~1 Hz and lack of toe-pinch reflex) throughout the duration of the surgery and recording. For detailed surgical methods, see Khan *et al.*¹⁶ For a subset of experiments, ketamine and xylazine boosters (4 mg/kg of ketamine plus 0.4 mg/kg of xylazine) were used instead of pentathiol. We did not observe any degradation of the linear model's performance between the two anesthesia protocols. For recordings during tracheotomized condition, respiration was monitored via a thermocouple (5TC-TT-K-40-36, Omega) placed outside the tracheal cannula going toward the lungs. For the reversible tracheotomy, the two tracheal cannulae were reconnected via a Y-shaped connector. The third arm of the connector was connected to a pressure sensor (HSCDRRN002NDAA3, Honeywell Sensing) to monitor the respiration.

For recordings, tetrodes were slowly lowered to the mitral cell layer and multi-unit activity was recorded either using: (i) a custom-built amplifier system (10,000× amplification, 300 Hz to 6 KHz band pass filtered, sampling rate 32 KHz) or (ii) an Intan Technologies amplifier chip (RHA1016, 200× amplification, 300 Hz to 5 kHz band pass filtered, sampling rate 32 KHz). Single-unit data was extracted by spike sorting using MClust (MClust-3.5, A.D. Redish). The respiration waveform and the valve states of the suction, odor and exhaust valves were acquired simultaneously at 320 Hz.

All animal procedures were in accordance with NIH guidelines and were approved by Animal Care and Use Committees at the National Centre for Biological Sciences and Cold Spring Harbor Laboratory.

Stimulus presentation and trial structure. For recordings during the tracheotomized condition. Independent of the temporal structure, each stimulus presentation was flanked by a blank suction period (2–3 s) before and after the odor stimulus. A pre-odor suction period allowed for the measurement of a stable pre-odor baseline firing rate after decay of any suction induced transients in firing rate. The post-odor suction period allowed for measurement for the stimulus-induced response lasting after the stimulus.

Upon identification of an isolatable single unit, a test run was performed with randomly interleaved presentation of 200-ms-long odor pulses (12 repeats per odor). For each tested odor, a spike raster (time bin, 1 ms) and PSTH (time bin, 200 ms) was plotted using a custom-written MATLAB (Mathworks) program. A cell was identified as being responsive to an odor upon a significant change in firing rate during the odor period compared with the air period (analysis of variance, $P > 0.5$). For responsive units, responses were further recorded to various stimulus patterns of one or more odors, or different odor concentrations delivered in a randomly interleaved sequence (12 repeats per stimulus pattern). The peak concentration of each odor was kept constant for a given set of randomly interleaved stimulus patterns except when characterizing M/T responses across different odor concentrations. In the latter case, stimulus patterns at 2 or 3 different concentrations were randomly interleaved.

For any given recording site, the maximum recording duration was limited (1–1.5 h) by the frequency of anesthesia booster administration. This was done to minimize anesthesia-dependent drifts that would bias our analysis. Further, any cells that showed a substantial change in pre-odor baseline activity and/or spontaneous activity throughout the recording were discarded.

For free-breathing responses. To record the same cell's response in both free-breathing and tracheotomized conditions, the tracheal cannulae were carefully reconnected. Odor stimuli were delivered as 4-s-long pulses separated by 8-s-long intertrial intervals. Odor delivery was aligned to the exhalation onset of the respiration cycle preceding each odor period. At least 12 repeats were performed for each odor. Trials from different odors were randomly interleaved.

Preprocessing of M/T responses for the linear model. For responses during the tracheotomized condition. For each recorded odor-cell pair, we assigned spikes to individual trials by aligning to the suction onset. The stimulus pattern for each trial was identified using the odor valve time stamps as signatures, and trials were sorted by stimulus type (temporal pattern). For each stimulus pattern, the spikes were binned in 50-ms bins, and PSTHs were constructed by calculating the average firing rate across all repeats. The firing rate was smoothed by a 25-ms Gaussian window for display purposes but not for analysis.

For respiration-tuned responses. Using inhalation onset in each respiration cycle as a reference, spikes were assigned to individual respiration cycles. Using the odor valve state information in the acquisition program, respiration cycles were sorted into odor and air periods. For each respiration cycle, spikes were binned in 50-ms time windows. As the odor delivery was triggered on the exhalation onset of the respiration cycle preceding each odor period, only the first inhalation cycle after odor onset was considered for analysis purposes. Odor-evoked and baseline respiration-tuned responses were calculated by averaging across cycles within odor and air periods, respectively.

Linear model and response predictions. Linear model for M/T responses to time-varying odor patterns. We modeled the output firing rate response of a cell to a time-varying stimulus pattern of a given odor at a fixed maximum odor concentration using a simple linear model and a static threshold.

$$PFR_{i,\text{unrectified}}(t) = \int_{-\infty}^{+\infty} K(x) \cdot O_i(t-x) \cdot dx + \text{baseline} \quad (1)$$

$$PFR_i(t) = \begin{cases} PFR_{i,\text{unrectified}}(t), & PFR_{i,\text{unrectified}}(t) > 0 \\ 0, & PFR_{i,\text{unrectified}}(t) \leq 0 \end{cases} \quad (2)$$

where $PFR_{i,\text{unrectified}}(t)$ = unrectified, predicted output firing rate of the cell to the i th stimulus pattern as a function of time (bins, 50 ms). $PFR_i(t)$ = rectified, predicted output firing rate of the cell to the i th stimulus pattern as a function of time (bins, 50 ms). $K(x)$ = odor kernel. Odor kernel was defined as the response of the cell to the shortest pulse of odor at the given maximum concentration (bins, 50 ms).

The duration of the shortest pulse was fixed at 50 ms so as to be slower than the output kinetics of our odor delivery system (average on kinetics, 40.1 ± 2.8 ms, **Supplementary Fig. 1b**). Accordingly, for all our analysis, the input and output firing rates and stimulus waveforms were binned at a resolution of 50 ms. The length of the response kernel was fixed at 2 s. This was defined by the maximum duration of the post-odor suction period. $O_i(t)$ = odor amplitude as a function of time measured via a PID for a given on/off sequence of the odor valve (bins, 50 ms). Baseline = mean firing rate of the cell in a 1-s suction window preceding odor onset and averaged across all trials and all stimulus patterns.

Kernel estimation via error minimization. Using the above model, we estimated the odor kernel by minimizing the least squared error between the predicted and experimentally observed output firing rates to a select set of stimulus patterns (training data set).

$$\text{Error} = \sum_{i=1}^N \sum_{t=0}^T (EFR_i(t) - PFR_{i,\text{unrectified}}(t))^2 \quad (3)$$

where $EFR_i(t)$ = experimentally observed firing rate to the i th stimulus, averaged across all trials (bins, 50 ms). $PFR_{i,\text{unrectified}}(t)$ = unrectified, predicted output firing rate of the cell to the i th stimulus pattern as a function of time (bins, 50 ms). Use of the unrectified predictions was essential to constrain the negative parts of the kernel, particularly for responses with strong odor-evoked inhibition in which the response itself provides little information (firing rate floors to zero) to efficiently constrain the kernel prediction.

The error minimization employed the Levenberg-Marquardt algorithm and was done using the `lsqcurvefit` function in MATLAB (Mathworks). High-frequency components in the kernel obtained as an artifact of the deconvolution operation were smoothed out using the Savitzky-Golay filter function (order 4, window size 11) in MATLAB only for display purpose. We verified that the fit quality of our response predictions was unaffected by smoothing the kernel.

The training data set used for kernel estimation consisted of half the stimulus patterns presented for a given cell-odor pair. The remaining half of the stimulus patterns was used as the cross-validation set to assess the model performance. We then repeated the process by swapping the training and cross-validation data sets. In this manner, we obtained two model performance estimates for each stimulus—one when the stimulus was part of the training set and the other when the stimulus was part of the cross-validation set (**Fig. 2d–f**).

On average, stimuli used for error minimization included individual odor pulses of 2 or 3 different durations (50, 100, 200, 500, 1,000 or 2,000 ms), non-overlapping paired pulses of 200 ms each with 2 or 3 different interpulse intervals

(50, 100, 200, 500 or 1,000 ms) and pseudo-random fluctuating stimulus spanning a total duration of 5 s. We found that for a majority of cases, the predicted kernel did not substantially depend on the choice of the training data set. However, for odor-evoked responses that had high inhibition content (frequent flooring of the firing rate to zero), including stimuli with high-frequency content in the training data set, substantially boosted the accuracy of kernel prediction.

Linear model for summation of M/T responses for binary odor stimuli. We modeled the output firing rate of a cell to a binary combination of two time-varying odor stimuli, presented either simultaneously or with a temporal offset (τ), as the sum of responses to the two stimuli presented individually.

$$PFR_{AB,unrectified}(t + \tau) = PFR_{A,unrectified}(t) + PFR_{B,unrectified}(t + \tau) + \text{baseline} \quad (4)$$

$$PFR_{AB}(t) = \begin{cases} PFR_{AB,unrectified}(t), & PFR_{AB,unrectified}(t) > 0 \\ 0, & PFR_{AB,unrectified}(t) \leq 0 \end{cases} \quad (5)$$

where $PFR_{AB,unrectified}(t + \tau)$ = unrectified, predicted firing rate to a binary combination of odor A and odor B stimulus patterns presented with a temporal offset of τ or simultaneously ($\tau = 0$). $PFR_{AB}(t + \tau)$ = rectified, predicted firing rate to a binary combination of odor A and odor B stimulus patterns presented with a temporal offset of τ or simultaneously ($\tau = 0$). $PFR_{A,unrectified}(t)$ = unrectified, predicted firing rate to odor A stimulus pattern presented individually. $PFR_{B,unrectified}(t)$ = unrectified, predicted firing rate to odor B stimulus pattern presented individually. Baseline = mean pre-order baseline firing rate. $PFR_{A,unrectified}(t)$ and $PFR_{B,unrectified}(t)$ were calculated by modifying equation (1) as follows:

$$PFR_{A,unrectified}(t) = \int_{-\infty}^{+\infty} K_A(x) \cdot O_A(t-x) \cdot dx \quad (6)$$

$$PFR_{B,unrectified}(t) = \int_{-\infty}^{+\infty} K_B(x) \cdot O_B(t-x) \cdot dx \quad (7)$$

K_A and K_B = estimated response kernel for odor A and B, respectively. O_A and O_B = stimulus pattern of odor A and B, respectively. To calculate $PFR_{A,unrectified}(t)$ and $PFR_{B,unrectified}(t)$, we used response kernels that were estimated using trials in which only one of the two odor patterns were presented. The binary odor responses were never used for kernel estimation.

Linear model for respiration-tuned response of M/T cells. We defined the odor-evoked, respiration-tuned response $EFR_O(t)$ of the cell as the odor-evoked firing rate of the cell during the first respiration cycle after odor onset (averaged across all odor periods), as a function of t :

$$EFR_O(t) = \text{odor-evoked firing rate as a function of time (bins, 50 ms)}$$

The baseline respiration tuning $EFR_A(t)$ was defined as firing rate of the cell during the penultimate respiration cycle in the air period preceding the odor onset (averaged across all air periods), as a function of t :

$$EFR_A(t) = \text{baseline firing rate of the cell as a function time (bins, 50 ms)}$$

We modeled the odor-evoked, respiration-tuned response of a cell as the sum of the baseline tuning $EFR_A(t)$ and the odor-driven change in the cell's firing ($OFR(t)$) as a function of respiration.

$$PFR_O(t) = EFR_A(t) + OFR(t) \quad (8)$$

The odor-driven change in the cell's firing rate $OFR(t)$ was calculated as the convolution of the odor-response kernel (estimated from responses in the tracheotomized rat) and the respiration waveform measured by the pressure sensor during free breathing.

$$OFR(t) = \int_{-\infty}^{+\infty} K_{\text{odor}}(x) \cdot R(t-x) \cdot dx \quad (9)$$

where $OFR(t)$ = predicted odor-driven change in firing rate; K_{odor} = odor-response kernel of the cell, estimated from responses during the tracheotomized

condition; and $R(t)$ = respiration waveform, averaged across all respiration cycles as measured via a pressure sensor, thresholded (to discard exhalation component) and scaled to maximize correlation between observed and predicted respiration-tuned odor responses.

$$PS_{\text{rectified}}(t) = \begin{cases} PS(t), & PS(t) > 0 \\ 0, & PS(t) \leq 0 \end{cases} \quad (10)$$

$$R(t) = 0.07 * \left(\frac{PS_{\text{rectified}}(t)}{\max(PS_{\text{rectified}})} \right) \quad (11)$$

where $PS(t)$ = respiration dynamics measured by the pressure sensor, as a function of time (bins, 50 ms). The scaling factor of 0.07 was determined empirically and was found to be surprisingly consistent across all rats. Of note, however, is that in practice this scaling factor depends on amplifier gain of the pressure sensor, tracheal tubing diameter, etc., and may not reflect the absolute transform of nasal pressure to flow rates.

Similar to the model predictions for the binary odor stimuli, the odor-response kernels were estimated using only the responses during the tracheotomized condition. The free-breathing data were never used for kernel estimation.

Estimating the quality of the model predictions for M/T cell odor responses during the tracheotomized condition. We used three different metrics to describe the model's performance across all cell-stimulus pairs. The different metrics are described below. All analysis described in the subsequent sections is based on comparisons of the predicted firing rate (predicted at time resolution of 50 ms) to the observed firing rate, also binned at a time-resolution of 50 ms.

Comparison of residual errors with the intertrial variability. We used a metric previously described by Geffen *et al.*³⁴ Briefly, for a given cell-odor pair, for each stimulus pattern we calculated the following parameters: residual (R_i) = mean squared error of the fit for the i th stimulus pattern. Noise (N_i) = variance of the experimentally observed firing rate to the i th stimulus pattern. Signal (S_i) = average response amplitude to the i th stimulus pattern.

$$R_i = \left\langle \left(PFR_i(t) - EFR_i(t) \right)^2 \right\rangle_t \quad (12)$$

$$N_i = \left\langle \left\langle \left(EFR_{i,j}(t) - EFR_i(t) \right)^2 \right\rangle_j \right\rangle_t \quad (13)$$

$$S_i = \left\langle \left(EFR_i(t) - EFR_i \right)^2 \right\rangle_t \quad (14)$$

where $PFR_i(t)$ = predicted output firing rate of the cell to the i th stimulus pattern. $EFR_{i,j}(t)$ = experimentally observed firing rate to the i th stimulus in the j th trial. $EFR_i(t)$ = experimentally observed firing rate as a function of time and averaged across all trials.

$$= \left\langle EFR_{i,j}(t) \right\rangle_j$$

EFR_i = mean firing rate, averaged across all trials and across all time bins

$$= \left\langle EFR_i(t) \right\rangle_t$$

For each stimulus pattern, we then plotted the ratio of $\sqrt{S_i/R_i}$ and $\sqrt{S_i/N_i}$ (Figs. 2d, 3d and 4d). A good fit was indicated by residual errors less than the intertrial variability (left-tail t -test, $P > 0.05$) (Supplementary Figs. 3a and 6a).

Temporal correlation of predicted mean firing rate to the observed mean firing rate. In a regime of high trial-to-trial variability (poor signal-to-noise ratio), residuals smaller than noise may not necessarily imply that the predicted response is a good estimator of the mean response profile of the cell. To provide a more direct measure of the match between the model output and observed responses, we calculated the Pearson correlation coefficient (r) between the predicted firing rate and the average observed firing rate across trials for each cell-stimulus pair (Figs. 2e, 3e and 4e).

$$r_i = \frac{\text{cov}(EFR_i(t), PFR_i(t))}{\sqrt{\sigma_{EFR_i(t)} \cdot \sigma_{PFR_i(t)}} \quad (15)$$

where r_i = Pearson correlation coefficient between the predicted and observed average response (as a function of time) to the i th stimulus. $EFR_i(t)$ = observed average firing rate response to the i th stimulus across t . $PFR_i(t)$ = rectified, predicted average firing rate response to the i th stimulus across t . $\sigma_{EFR_i(t)}$ = s.d. of the observed average firing rate response to the i th stimulus across t . $\sigma_{PFR_i(t)}$ = s.d. of the predicted average firing rate response to the i th stimulus, across t . We further compared r with the average pairwise correlation observed across trials (r_{trial}) (Supplementary Figs. 3b and 6b).

Fraction of stimulus-related response variance explained by the model predictions. An absolute measure of a model's success is difficult to estimate because of the presence of intertrial variability in experimental observations. A zero residual error (or $r = 1$) is theoretically impossible to achieve. This is because even the best model can only account for the stimulus-related variance in the observed response, still leaving out the variance induced by noise factors. We thus calculated an alternative metric to gauge the fraction of stimulus-related variance in the observed response explained by our model (fraction of variance explained, *fve*) (Figs. 2f, 3f and 4f). To account for the noise-induced variance, we corrected the residual error for each prediction (R_i) by subtracting out the expected noise-induced variance in the observed average firing rate response (η_i).

$$fve_i = \frac{S_i - (R_i - \eta_i)}{S_i} \quad (16)$$

where

$$S_i = \left\langle (EFR_i(t) - EFR_i)^2 \right\rangle_t \quad \text{from equation (14)}$$

$$R_i = \left\langle (PFR_i(t) - EFR_i(t))^2 \right\rangle_t \quad \text{from equation (12)}$$

$$\eta_i = \left\langle \left\langle (fEFR_{i,j}(t) - EFR_i(t))^2 \right\rangle_t \right\rangle_j \quad (17)$$

where η_i = expected noise-induced variance in the observed average firing rate response. $fEFR_{i,j}(t)$ = mean firing rate response (across time) to the i th stimulus obtained by bootstrap selection (j th time) of an equal number of trials from the original trial set with replacement. $fEFR_{i,j}(t)$ is a 'fake' set of mean firing rate vectors generated by randomly selecting (j times, $j = 100$) with replacement n trials from the original set of n trials for each stimulus. As a result, each fake mean is obtained by averaging the same number of trials (n), as in the original data set, with some redundancy in trials selected in any given iteration.

Interpreting the *fve* metric:

fve = 0: *fve* value of 0 is obtained when the corrected residual error ($R_i - \eta_i$) between the observed and predicted response is equal to the stimulus-induced variance in the observed response, indicating poor model performance. In rare cases (29/2062 for single odor predictions, and 35/314 for mixture predictions), *fve* values were negative. This can result from very large residuals or very small signal variance (weak responses) or both. To constrain the model's worst performance at 0, negative *fve* values were thresholded at zero for all analysis purposes.

$$fve_i = \begin{cases} fve_i, & fve_i > 0 \\ 0, & fve_i \leq 0 \end{cases}$$

fve = 1: *fve* value of 1 is obtained when the corrected residual error ($R_i - \eta_i$) is 0. This implies that the error between the observed and predicted responses can be fully accounted for by noise in the observed responses, indicating good model performance. The *fve* value may exceed 1 in cases of over-fitting (model predictions also account for some noise-related variance in the data).

Estimating the quality of the model predictions for respiration-tuning M/T cell odor responses during the free-breathing condition. For analysis of model predictions of respiration-tuned responses, we only considered the first respiration cycle following odor onset. We calculated r and the ratio of $\sqrt{S_i}/R_i$ and $\sqrt{S_i}/N_i$ using equation (15) and equations (12–14), respectively. We did not perform the variance analysis on this set of data. This is because the variance of the model predictions for respiration tuning are not only determined by the convolution of the odor kernels with the stimulus waveform (respiration) but also by constraints on accurate estimation of the baseline respiration-tuned firing rate of the cell during the air period. The latter substantially inflates the variance of the predicted response vector even though the correlation between the observed and predicted responses remains high.

Calculation of preferred firing phase and latency of odor response. We extracted representative sniff waveforms in awake, behaving rats from previously published data (Fig. 6a from ref. 37). We selected 1-s long bouts of slow and rapid sniffing from this data. For each of these bouts, we discarded the exhalation periods and binned the waveforms into time bins of 50 ms to match the temporal resolution of the respiration waveforms to that of the estimated odor kernels in our data set. We obtained the firing rate response of a cell during slow and fast sniffing by convolving each M/T cell odor kernel with the slow and fast sniff bouts, respectively. Response latency (Fig. 6a) was calculated as time to first peak in firing rate from the onset of inhalation³⁷. We did not explicitly model the change in baseline respiration tuning at different sniff frequencies. Baseline respiration tuning has been shown to be modulated across slow and fast sniffs in a manner similar to the odor-evoked component of the response, producing sniff-invariant latency of peak firing rate after inhalation onset. We thus expect that adding the baseline respiration tuning will not substantially alter our conclusions.

The preferred firing phase (Fig. 6b) was calculated from the predicted respiration-tuned response for each M/T cell odor kernel, using the average respiration waveform measured via a pressure sensor during 1-Hz breathing in anesthetized rats in our experiments. The preferred phase was defined as the phase of the respiration cycle at which the firing rate was maximum³⁸. We found that the distribution of preferred phases was unaffected by the absolute frequency of the respiration cycle used for convolution.

Classification and characterization of odor kernels. To parameterize the M/T cell odor kernels, we described them as Gabor functions with 5 independent parameters (a, t, τ, f, ϕ).

$$K(t) = a \times e^{\left(\frac{-(t-\tau)}{w} \right)^2} \times \cos(2\pi(f+t-\tau) + \phi) \quad (18)$$

For each M/T cell odor kernel, we found the best set of 5 parameters to minimize the least squared error between the parameterized kernel and the estimated kernel from the linear model. For classification of kernels, we calculated the pairwise distance between every pair of parameterized kernels.

$$\text{Dist}_{i,j} = 1 - \max(\text{crosscorr}(K_i, K_j)) \quad (19)$$

Using the dendrogram function in MATLAB, we hierarchically clustered the kernels based on average linkage to obtain 8 families. Families with less than 2 kernels were discarded.

For display purposes only (Fig. 6c), we normalized each kernel by its peak amplitude and aligned kernels within each family by time of peak. Kernel latency (Fig. 6c) was calculated as the time to first peak in the second derivative of the kernel. Kernel duration (Fig. 6c) was calculated as the time between the first and last peak in the second derivative of the kernel.

No statistical method was used to predetermine sample size.

A **Supplementary Methods Checklist** is available.